photonics

MDPI

Article

Design, Calibration, and On-Site Validation of an LCVR-Driven Fast-Tunable Lyot Filter for the YOGIS Coronagraph

Tengfei Song [1,2,†], Yu Liu [3,†], Xuefei Zhang [1,2], Mingyu Zhao [1,2] and Zhen Li [4,*]

[1] Yunnan Observatories, Chinese Academy of Sciences, Kunming 650216, China; stf@ynao.ac.cn (T.S.)
[2] Yunnan Key Laboratory of Solar Physics and Space Science, Kunming 650216, China
[3] College of Physical Science and Technology, Southwest Jiaotong University, Chengdu 611756, China; lyu@swjtu.edu.cn
[4] School of Astronomy and Space Science, Nanjing University, Nanjing 210093, China
* Correspondence: lizhen@nju.edu.cn
† These authors contributed equally to this work.

Abstract

The Lyot filter, a fundamental element of the Yunnan Observatories Coronagraph Green-line Imaging System (YOGIS) at Lijiang Observatory, utilizes a Liquid Crystal Variable Retarder (LCVR) for swift electrical modulation. This filter allows for precise observations of the coronal green line (Fe XIV, central wavelength 5303 Å) with a narrow full-width at half-maximum (FWHM) of 1 Å and enables rapid adjustment of the transmission band wavelength. This feature aids in capturing the sky background intensity around the green line and images of two line wings (offset by ±0.45 Å from the central wavelength), crucial for determining the green line's Doppler shift. By employing sky background subtraction and processing line wing images, an improved signal-to-noise ratio (SNR) in coronal green line images is achieved. The YOGIS Lyot filter, an enhancement of the NOrikura Green-line Imaging System (NOGIS) filter, operates at a wavelength of 5303 Å, offers a wavelength tuning range of ±2 Å, and tunes within <60 ms. This study elucidates the filter's design principles, outlines essential calibration procedures, and validates its performance through on-site observations using the YOGIS.

Keywords: Lyot filter; coronagraph; LCVR; YOGIS

1. Introduction

Coronal observation is essential for studying solar activities and space weather, with coronagraphs being the primary instruments for such observations [1]. Coronagraphs utilize the occulting technique to block the central region of the solar disk, allowing telescopes to detect the fainter coronal radiation surrounding the Sun [1–4]. Ground-based coronagraphs often focus on specific emission lines with stronger signals, such as the "green line" (Fe XIV, 5303 Å) [5] and the "red line" (Fe X, 6374 Å), due to the weak coronal signals and susceptibility to Earth's atmospheric interference. Therefore, the development of reliable filters is crucial for high-quality coronagraph imaging. These filters not only provide the necessary narrow-band central wavelength (typically around 1 Å) for observing coronal lines but also allow for tuning the transmission band for multi-band observations and effective sky background subtraction. This tuning results in coronal images with a higher signal-to-noise ratio (SNR) [6].

Four mainstream optically tunable filters are widely employed in observation systems: Liquid Crystal Tunable Filters (LCTF) [7–9], Acousto–Optic Tunable Filters (AOTF) [10],

Check for updates

Received: 29 November 2025
Revised: 31 December 2025
Accepted: 9 January 2026
Published: 16 January 2026

Copyright: © 2026 by the authors. Licensee MDPI, Basel, Switzerland. This article is an open access article distributed under the terms and conditions of the Creative Commons Attribution (CC BY) license.

Volume Bragg Grating-Based Tunable Filters (LLTF) [11], and Fabry–Perot Tunable Filters (FPTF) [12]. Their wavelength tuning hinges on distinct optical mechanisms, leading to notable differences in key performance metrics. Specifically, LCTFs achieve wavelength selection via liquid crystal electrically controlled birefringence, offering advantages of no mechanical transmission, fast tuning, and compact size. However, constrained by liquid crystal molecular arrangement, they have small clear apertures and poor spectral stability in wide-band tuning. AOTFs modulate light via acousto–optic interaction, featuring rapid tuning, wide bandwidth, and strong anti-vibration capability, but suffer from high insertion loss, polarization sensitivity, and insufficient narrow-band precision for high-accuracy solar spectral observations. LLTFs rely on volume Bragg grating diffraction, boasting high diffraction efficiency and narrow bandwidth, yet their angle-dependent mechanical tuning results in a limited range, slow response, and incompatibility with real-time dynamic solar observation. FPTFs realize wavelength selection via Fabry–Perot interferometry (adjusting the air gap between parallel reflectors), with a simple structure and easy integration, but demand ultra-high mechanical precision and exhibit strong vibration sensitivity, limiting their application in telescopes requiring frequent rotation [9]. For coronal observations, the Liquid Crystal Variable Retarders (LCVRs) Lyot filter (a type of LCTF) [6,13,14] is selected, with core justifications as follows: First, it exhibits enhanced stability and environmental adaptability. By replacing the mechanically rotating half-wave plates in traditional Lyot filters with LCVRs, it eliminates mechanical mechanisms, avoiding vibration sensitivity and long-term stability degradation due to mechanical wear, and adapting to frequent telescope rotation and complex outdoor solar observation environments [15,16]. Second, it achieves superior tuning efficiency: LCVRs enable fast, precise wavelength tuning via voltage-controlled phase retardation, with significantly improved response speed and controllable accuracy compared to traditional mechanical tuning, meeting real-time spectral capture needs for dynamic solar activities (LCVR optical response time < 40 ms; multi-stage filter switching time < 100 ms). Third, its optical performance matches coronal observation requirements: inheriting the large clear aperture of traditional Lyot filters to ensure sufficient light flux for weak coronal signals (e.g., Fe XIV 530.3 nm green line). It also provides excellent polarization measurement and high-quality spectral imaging, critical for in-depth solar physics research [9,13,17]. Fourth, it offers favorable structural integration: without mechanical components, it is more compact than bulky filters (e.g., some LLTFs, FPTFs), facilitating integration with coronagraphs and reducing system complexity and cost.

The Yunnan Observatories Coronagraph Green-line Imaging System (YOGIS) [18–20] is a 10 cm internal-occulting coronagraph located at Lijiang Observatory [21]. This system was developed through collaboration between the Yunnan Observatories and the National Astronomical Observatory of Japan (NAOJ) and is specifically designed to observe the coronal green line within the range of $1.03R_{\odot} \sim 2.5R_{\odot}$. YOGIS represents an advancement over the NOrikura Green-line Imaging System (NOGIS) [22] originally created by NAOJ. The system employs an LCVR-driven fast-tunable Lyot filter (YOGIS-Lyot filter), which improves upon the Lyot filter used in NOGIS. Notable specifications of the YOGIS-Lyot filter include an operating wavelength of 5303 Å, a full-width at half-maximum (FWHM) of 1 Å, a wavelength tuning range of ± 2 Å, and a tuning time of less than 60 ms. This paper provides a comprehensive overview of the optical design, essential technical calibration procedures, and electronic control system of the YOGIS-Lyot filter. Additionally, it presents the outcomes of on-site validation observations conducted with YOGIS, illustrating the successful capture of high-SNR images of the coronal green line.

https://doi.org/10.3390/photonics13010076

2. Design of the YOGIS-Lyot Filter

2.1. Design Principle

The YOGIS-Lyot filter operates on the principle of polarization interference, which underpins its narrow-band filtering and wavelength tuning capabilities [13]. Initially, light incident on the filter is polarized before traversing a series of birefringent elements, commonly known as waveplates or retarders. These waveplates create a controlled phase difference between the ordinary (o) light and extraordinary (e) light, resulting in constructive or destructive interference at various wavelengths [23]. This interference phenomenon facilitates the selection of specific wavelengths or wavelength ranges by optimizing the orientation and thickness of the waveplates, as illustrated schematically in Figure 1.

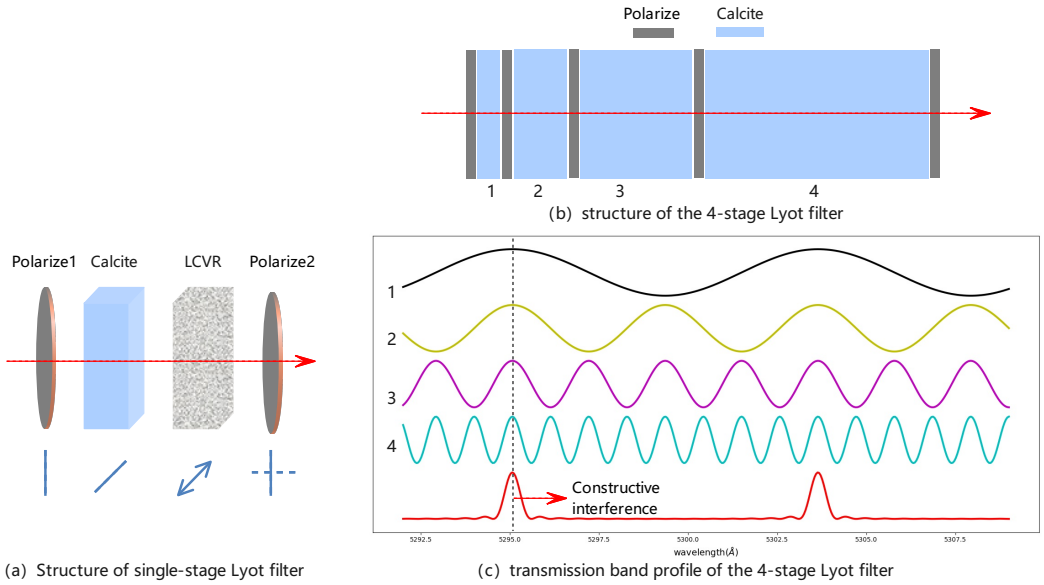


Figure 1. Schematic diagram of the Lyot filter.

A single-stage LCVR-based tunable Lyot filter unit, as illustrated in Figure 1a, typically comprises two polarizers with their principal axes oriented either parallel or orthogonal to one another, a birefringent crystal aligned with its fast axis at 45°, and an LCVR. For incident light with intensity I_0, the intensity I of the emergent light after traversing the unit is expressed as [9,13,14]:

$$I = \frac{1}{2} I_0 cos^2(\delta_C + \delta_{LCVR}) \quad (1)$$

where δ_C represents the phase retardation induced by the birefringent crystal, which varies with wavelength and crystal thickness under constant temperature conditions. δ_{LCVR} indicates the phase retardation produced by the LCVR, which depends on both wavelength and applied voltage. To achieve an ultra-narrow FWHM, Lyot filters are typically constructed by cascading multiple single-stage units, with the FWHM of each subsequent unit being doubled. Figure 1b,c illustrate the structural diagram and transmission band profile of a four-stage Lyot filter, respectively. By extending and normalizing Equation (1), the transmission band profile of an n-stage Lyot filter can be expressed as:

$$T = \prod_{i=1}^{n} cos^2[\frac{\pi d_i (n_o - n_e)}{\lambda} + \delta_{LCVR}(V_i)] \quad (2)$$

Here, d_i represents the total thickness of the two birefringent crystals in the i-th stage, λ denotes the wavelength, and n_o and n_e refer to the refractive indices of the birefrin-

gent crystal for ordinary light (o-light) and extraordinary light (e-light) at the operating temperature, respectively.

2.2. Filter Bandwidth Properties

As can be inferred from Equation (2), the half-width of the transmission band is determined by the units with thickness d_i. Let $\theta = \frac{\pi \mu d_i}{\lambda}, (\mu = (n_o - n_e))$; differentiating this with respect to wavelength yields the following [13]:

$$\Delta\lambda_{\mathrm{HW}} = \frac{\lambda_0^2}{2^n \mu d_1} \frac{1}{(1 - \frac{\lambda}{\mu}\frac{\partial \mu}{\partial \lambda})} = \frac{\lambda_0^2}{2^n \mu d_1} \cdot Q \tag{3}$$

To characterize the width between half-power points, by substituting the 50% peak transmittance condition into the Gaussian-like transmission profile of Lyot filters, and fitting this model to the actual filter response, the conversion expression is derived as follows [13]:

$$\Delta\lambda_{\mathrm{FWHM}} = 0.886\Delta\lambda_{\mathrm{HW}},\ Q = \frac{1}{(1 - \frac{\lambda}{\mu}\frac{\partial \mu}{\partial \lambda})} \tag{4}$$

The coefficient 0.886 stems from numerical fitting of the Lyot filter's characteristic quasi-Gaussian passband. Q denotes the half-width dispersion correction factor, which is generally set to $Q = 1$ under ideal conditions. Naturally, Q is affected by the inhomogeneity of the birefringent crystal; however, for the YOGIS case—narrow-band modulation focused on a single wavelength—the spectral interval of interest is sufficiently limited. Within this narrow range, Q exhibits minimal variation (remaining near 1 even for typical high-quality birefringent crystals), such that approximating Q as 1 introduces no significant errors to the transmission band's FWHM. In actual assembly, the thickness d of the birefringent crystal has a more significant influence. Therefore, it is crucial to precisely control the thickness of each Lyot stage in accordance with the designed FWHM requirements of the filter.

For the first stage of the YOGIS-Lyot filter, which requires a transmission band centered at 5303 Å with a half-width of 1 Å, adopting calcite as the birefringent material (with $\mu = 0.17418$) leads to a calculated thickness of $d_1 = 8.9205$ mm, corresponding to an actual FWHM of $\Delta\lambda_{\mathrm{FWHM}} = 1.00223$ Å. This serves as an important reference formula for practical assembly processes.

2.3. Optical Configuration

The YOGIS-Lyot filter is specifically engineered to target the coronal green line. Informed by the spectral characteristics of this line and the demands of high-precision observation, the filter features a FWHM of 1 Å for its transmission band. Through optical simulation and parameter optimization, the filter employs a cascaded architecture comprising four Lyot units and two LCVRs. The FWHMs of the four Lyot units are 1 Å, 2 Å, 4 Å, and 8 Å, respectively (Figure 2 presents the detailed optical hardware structure of the YOGIS-Lyot filter).

Calcite has been selected as the birefringent crystal material, and the LCVRs are custom-manufactured by Meadowlark Optics [24]. Each Lyot unit consists of two birefringent crystals and one half-wave plate, which effectively expands the filter's field of view. All polarizers, half-wave plates, and birefringent crystals are meticulously arranged at specific angles and in precise optical sequences to ensure the stability of polarization interference. The tunable Lyot units integrated with LCVRs, specifically the 1 Å and 2 Å units, are positioned at the front and rear ends of the filter, respectively, facilitating efficient wavelength tuning and phase control. Given the high temperature sensitivity of optical components, where temperature fluctuations can induce central wavelength drift, the entire

optical assembly is housed in a thermostatic control chamber maintained at 40.6 °C. A super-narrowband hard-coated prefilter, manufactured by Andover Corp. (Salem, MA, USA), features a FWHM of 10 Å. This prefilter achieves a transmittance exceeding 80% near the 5303 Å emission line while suppressing the intensity of non-target transmission bands to below 10%. The thermostatic control system and the electronic control system for the LCVRs are interconnected and regulated through reserved cable interfaces. The filter boasts a compact and lightweight design, allowing for seamless integration into the YOGIS observation system. Key optical and performance parameters of the YOGIS-Lyot filter are summarized in Table 1.

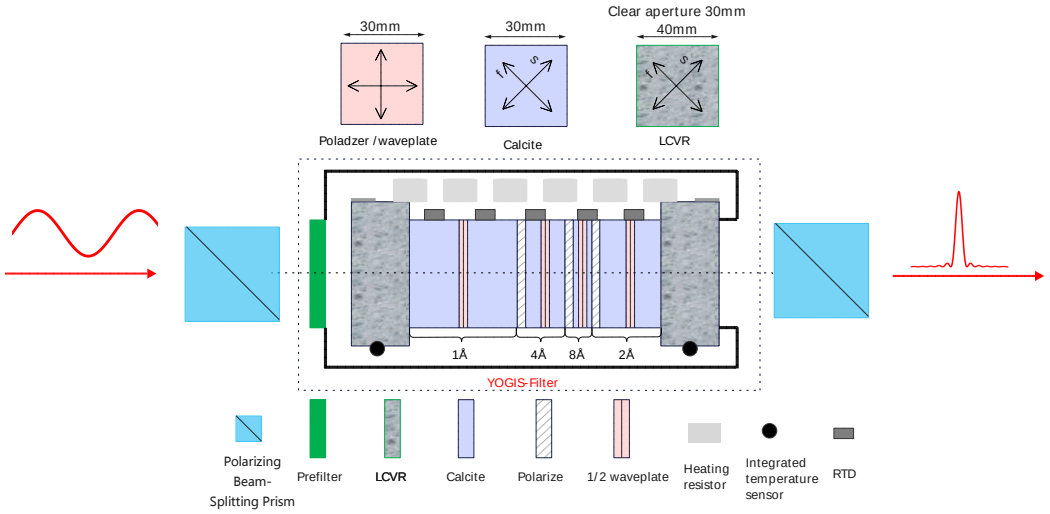


Figure 2. Optical structure of YOGIS-Lyot filter. At the entrance and exit pupils of the filter, there are two Polarizing Beam-Splitting Prisms (PBS Prisms). One function of the PBS Prisms is to serve as the entrance and exit polarizers of the filter; the other function is to split the light beam to meet the observation requirements of different wavelength bands, such as the *Hα* band.

Table 1. Key specifications of the YOGIS-Lyot filter.

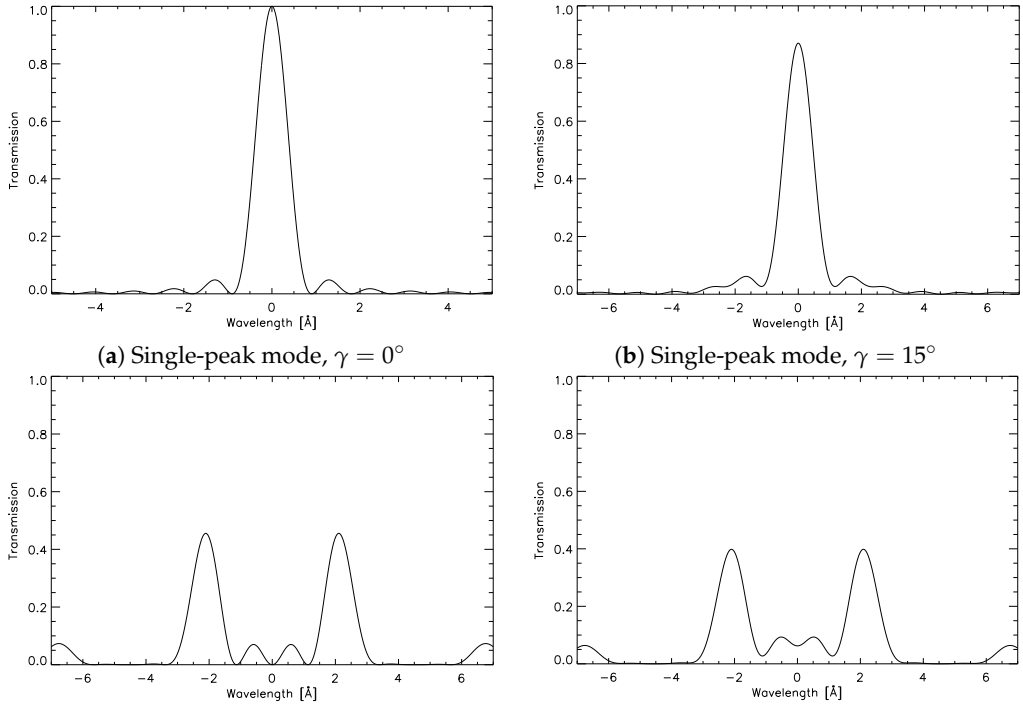
Parameter	Value
Central Wavelength	5303 Å
FWHM (Full-Width at Half-Maximum)	1 Å
Effective Clear Aperture	30 mm
Free Spectral Range (FSR)	2 Å
Wavelength Tuning Time	<60 ms
Thermostatic Chamber Operating Temperature	40.6 °C
Temperature Stability Precision	0.01 °C

2.4. Effects of Orientation Errors of Polarizers and Wave Plates

Equation (2) assumes an ideal cosine-squared transmission for each Lyot stage. In practice, crystal imperfections, polarizer leakage, and residual LCVR retardance errors lead to reduced sidelobe suppression compared to the ideal model. Let α denote the angle between the optical axis of the wave plate and the transmission axis of the pre-polarizer, and β denote the angle between the optical axis of the wave plate and the transmission axis of the filter unit. In the assembly process, unavoidable deviations will cause the aforementioned α and β to not strictly equal 45°. The YOGIS-Lyot filter consists of the following four stages: the thickest stage is placed at the front, and the second thickest stage at the rear. Specifically, for $k = 2$, $\beta \neq 45°$; for $k = 3$, $\alpha \neq 45°$. From Equation (2), we can derive the following:

$$T' = \cos^2\gamma - \cos(2\gamma)\sin^2\frac{\delta}{2} \quad (5)$$

where γ is the orientation error of a polarizer, and δ is the specific phase retardation angle of this stage. Obviously, compared with $T = \cos^2(\frac{\delta}{2})$, the peak position and period of the single-stage transmittance profile remain unchanged—only the transmittance magnitude varies. The peak position of the total transmittance also stays unchanged, but its magnitude decreases, while the wings of the peak rise (i.e., more light from other wavelength bands will leak through), as illustrated in Figure 3. Figure 4 illustrates the measured transmission band curves when the polarizer is misaligned by approximately 10°. Therefore, it is critical to maximize the positional accuracy of polarizers during assembly. Using the photometric scanning method, the deviation can generally be controlled within 1°.



(**a**) Single-peak mode, $\gamma = 0°$ (**b**) Single-peak mode, $\gamma = 15°$

(**c**) Dual-peak mode, $\gamma = 0°$ (**d**) Dual-peak mode, $\gamma = 15°$

Figure 3. Influence of Polarizer Angle: Left is the ideal case at 45°; Right is the case where two LCVR tunable stages have a 15° deviation from 45°.

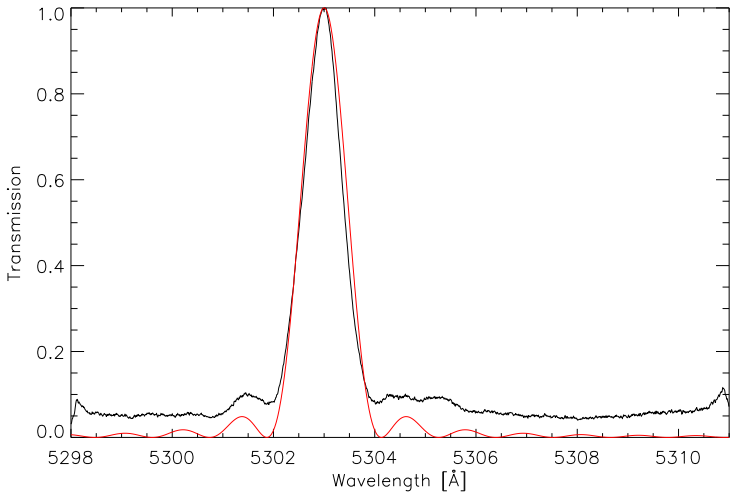


Figure 4. Comparison between measured and theoretical transmission band curves when the polarizer is misaligned by approximately 10°. Red: Theoretical transmission band curve. Black: Measured transmission band curve with 10° polarizer deviation. Misalignment of the polarizer primarily affects the SNR of the entire filter.

2.5. Transmission Band Wavelength Tuning

The rapid and accurate adjustment of the transmission band wavelength of the YOGIS-Lyot filter is facilitated by the electrically controlled birefringence effect of nematic liquid crystals in LCVRs. This capability for tuning removes the necessity for mechanical adjustments, allowing for swift transitions between target wavelengths. Such rapid switching is essential for observing the coronal green line, subtracting sky background, and calculating Doppler shifts.

2.5.1. Tuning Mechanism

According to the polarization interference principle (Section 2.3), the central wavelength of the transmission band is determined by the total phase retardation ($\delta_C + \delta_{LCVR}$) within each Lyot unit. In the case of fixed birefringent crystals, where δ_C remains stable at a constant temperature, tuning is accomplished by modulating δ_{LCVR} through adjustments to the voltage applied to the LCVRs. This voltage modulation affects the birefringence of the liquid crystal molecules in the LCVRs, thereby shifting the interference condition that establishes the central wavelength of the transmission band.

The quantitative relationship between the wavelength shift ($\Delta\lambda$) and the LCVR-induced phase retardation change ($\Delta\delta$) is described by:

$$\Delta\lambda = \frac{\lambda_0^2}{\pi d_0 (n_o - n_e)} \Delta\delta \tag{6}$$

where $\lambda_0 = 5303$ Å (central wavelength of the coronal green line), d_0 is the total thickness of birefringent crystals in the tunable Lyot units, and $n_o - n_e$ is the birefringence of calcite at the operating temperature (40.6 °C). This equation provides the theoretical basis for deterministic wavelength tuning.

2.5.2. LCVR Configuration and Phase Control

To achieve flexible and precise tuning, two LCVRs are strategically placed at the entrance and exit pupils of the filter (Figure 2), independently controlling the phase of the sinusoidal transmission curves of the 1 Å and 2 Å Lyot units. This configuration allows for two key tuning capabilities:

- Independent phase adjustment: Each LCVR modulates the phase of its corresponding Lyot unit, enabling targeted shifts in the transmission band without affecting other stages;
- Proportional phase modulation: Maintaining a 2:1 ratio of phase shifts between the 1 Å and 2 Å units ensures a single transmission peak that can be tuned within the ±2 Å range, with minimal sideband leakage (Figure 5).

2.5.3. Transmission Band Modes and Application Scenarios

By adjusting the phase retardation combination of the two LCVRs, the filter supports three operation modes tailored to YOGIS's observation requirements (Figure 5):

1. Single-peak mode: Both Lyot units are phase-aligned to center the transmission peak at 5303 Å, enabling high-SNR imaging of the coronal green line core;
2. Dual-peak mode: A 180° phase shift is applied to the 2 Å Lyot unit, generating two symmetric peaks separated by 2 Å. This mode is used to measure the continuous spectrum of atmospheric scattered light (sky background) for subsequent subtraction;
3. Line-wing mode: By tuning the phase shift ratio of the two LCVRs, the single transmission peak is offset by ±0.45 Å relative to 5303 Å, capturing images of the green line's wings. These images are critical for calculating the Doppler shift of coronal plasma.

2.5.4. Tuning Performance

The YOGIS-Lyot filter achieves a wavelength tuning range of ±2 Å around 5303 Å, effectively encompassing the green line core, ±0.45 Å wings, and sky background bands. The tuning time is less than 60 ms, primarily influenced by the relaxation time of liquid crystal molecules (approximately 50 ms) and the response delay of the electronic control system (less than 10 ms). This rapid tuning speed facilitates the sequential imaging of multiple bands (core, wings, background) within a time frame sufficiently short to prevent artifacts arising from solar activity evolution, thereby establishing a foundation for high-quality on-site validation.

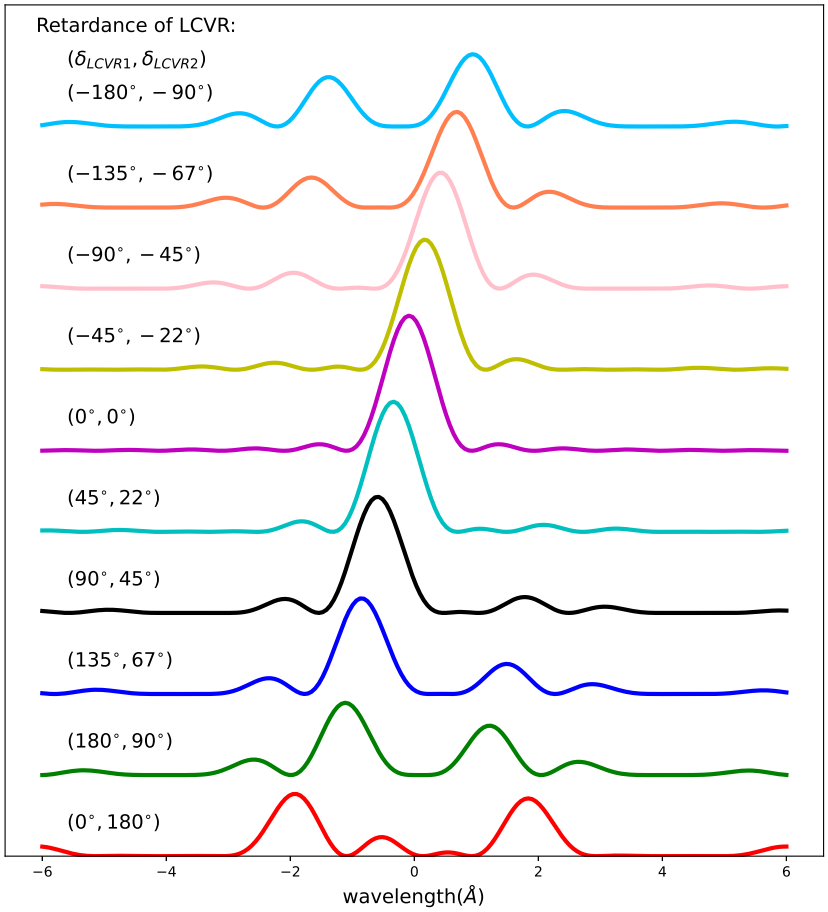


Figure 5. Theoretical transmission curves of the YOGIS-Lyot filter for different LCVR retardance combinations.

2.6. Calibration of LCVRs

As the essential component facilitating the "LCVR-driven fast-tunable" function of the YOGIS-Lyot filter, LCVRs demonstrate nonlinear relationships between phase retardation and driving voltage, which are further complicated by temperature sensitivity and wavelength dependence [16]. Uncalibrated LCVRs can introduce substantial errors in the tuning of the transmission band, thereby undermining the filter's capacity to capture high SNR images of the coronal green line. Consequently, high-precision calibration of LCVRs is imperative for ensuring reliable on-site operation with the YOGIS.

2.6.1. Rationale for Calibration

LCVRs rely on the collective orientation of internal nematic liquid crystal molecules to generate phase retardation, and their optical performance is susceptible to three key factors:

1. Voltage nonlinearity: The phase retardation (δ_{LCVR}) does not vary linearly with driving voltage (Figure 6), due to non-uniform liquid crystal alignment under electric fields. Without calibration, this would lead to deviations from target wavelengths (e.g., ±0.45 Å line wings).
2. Fast-axis misalignment: The LCVR's fast-axis azimuth (θ) may shift relative to the Lyot unit's polarization components, reducing interference contrast and lowering peak transmittance.
3. Temperature drift: The operating temperature of LCVRs differs from factory calibration conditions, altering liquid crystal birefringence and requiring temperature-compensated calibration.

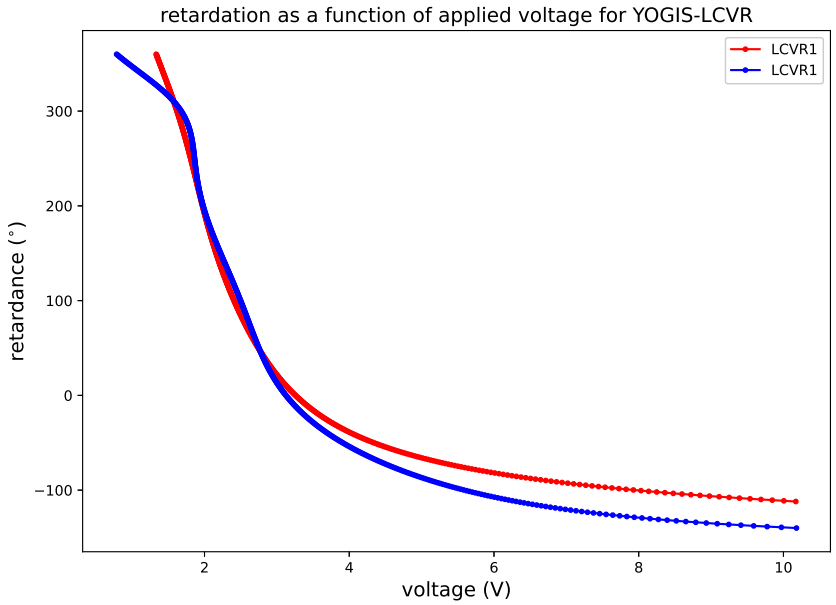


Figure 6. Relationship curve between LCVR phase retardation and control voltage of the YOGIS-Lyot filter at 5303 Å wavelength.

2.6.2. Calibration Methodology

Building upon the calibration protocol established for the NOGIS coronagraph, the LCVRs of the YOGIS-Lyot filter are calibrated using a Mueller Matrix Spectro-Polarimeter (MMSP), which serves as a gold-standard instrument for characterizing polarization devices in solar physics [23,25–27]. The MMSP system consists of a broadband light source (5200–5400 Å), a polarization generator equipped with precision rotating waveplates, a polarization analyzer integrated with a spectrometer, and a high-precision rotating stage with an angular resolution of 0.1°.

The calibration workflow proceeds as follows:

1. Sample Integration: The LCVR under test is mounted between the MMSP's polarization generator and analyzer, ensuring alignment with the optical axis.
2. Polarization Modulation and Data Acquisition: The rotating stage adjusts the fast-axis angles of the generator and analyzer, generating a sequence of polarized light inputs. The spectrometer records light intensity data across 5290–5310 Å (centered on 5303 Å) for each polarization state.
3. Mueller Matrix Extraction: Using Stokes vector inversion, the LCVR's full 4 × 4 Mueller matrix is derived from intensity data—quantifying δ_{LCVR} and θ at each wavelength.
4. Nonlinear Fitting: A seventh-order polynomial model is applied to fit the δ_{LCVR}-voltage relationship (Equation (7)), yielding calibration coefficients ($Coeff_A1$ for LCVR1, $Coeff_A2$ for LCVR2; Table 2). Temperature coefficients (LCVR1:

$tempA1 = [24.0093, 41.0141]$; LCVR2: $tempA2 = [24.9611, 40.5076]$) are further derived by repeating calibration at 38 °C, 40.6 °C, and 43 °C.

Table 2. Calibration coefficients of the YOGIS-Lyot filter.

Coeff_A1								
c_1	0.307	1.29×10^{-3}	-3.82×10^{-6}	2.17×10^{-8}	-6.39×10^{-12}	-5.74×10^{-13}	2.30×10^{-15}	-2.51×10^{-18}
c_2	0.324	1.48×10^{-3}	-4.66×10^{-6}	-7.12×10^{-9}	1.41×10^{-10}	7.02×10^{-13}	-6.75×10^{-15}	1.17×10^{-17}
Coeff_A2								
c_1	0.320	1.07×10^{-3}	-4.67×10^{-6}	2.55×10^{-9}	2.24×10^{-10}	-1.45×10^{-13}	-6.10×10^{-15}	1.36×10^{-17}
c_2	0.341	1.10×10^{-3}	-4.27×10^{-6}	1.09×10^{-8}	2.16×10^{-10}	-3.44×10^{-13}	-5.87×10^{-15}	1.62×10^{-17}

2.6.3. Calibration Outcomes and Application

- Performance metrics: At 5303 Å and 40.6 °C, the calibrated LCVRs achieve a maximum δ_{LCVR} of $\pm 180°$ (covering the ± 2 Å tuning range) with a fitting accuracy of $R^2 > 0.998$. Fast-axis deviation is reduced to <0.5°, minimizing polarization loss. Figure 6 shows the finally calibrated response curves of actual voltage versus phase retardation angle for the two LCVRs.
- On-site voltage calculation: During observation, the required δ_{LCVR} (e.g., 63° for −0.45 Å wing, Table 2) is converted to driving voltage via:
  1. Base voltage calculation using polynomial coefficients (Equation (7)):

$$va(i) = 1/\sum_k C_{ik} * \delta_{LCVR}^k = \frac{1}{C_{i0} + C_{i1} * \delta_{LCVR} + ... + C_{i1} * \delta_{LCVR}^7} \quad (7)$$

  2. Temperature compensation using $tempA1/tempA2$ and real-time temperature T_A (Equation (8)):

$$v_1 = CC(1) + CC(2) * TA1 \quad (8)$$

  This ensures precise δ_{LCVR} control for fast wavelength tuning.

2.7. Transmission Band Wavelength Calibration

While LCVR calibration accounts for nonlinearity at the component level, system-level deviations—resulting from temperature mismatches in the LCVR, fabrication errors in the calcite crystal, and misalignment during assembly—can still displace the filter's actual transmission band from its theoretical value. To accurately center the transmission band on the coronal green line and its wings, wavelength calibration of the transmission band is crucial, serving as the final calibration step prior to on-site validation.

2.7.1. Calibration Principle and Equipment

The calibration employs a high-resolution solar spectrometer (spectral resolution: 0.01 Å) to directly measure the transmission profile of the filter. Initially, the solar spectrometer captures the spectral curve of the coronal green line (5302–5304 Å) as the calibration spectrum using an outdoor solar heliostat. The YOGIS-Lyot filter is then integrated into the spectrometer's optical path, with a white light simulation source serving as the reference light source. Subsequently, the LCVRs are continuously modulated to derive the transmission band curve of the filter. Figure 7 presents a photograph of the experimental setup used for the transmission band wavelength calibration of the YOGIS-Lyot filter.

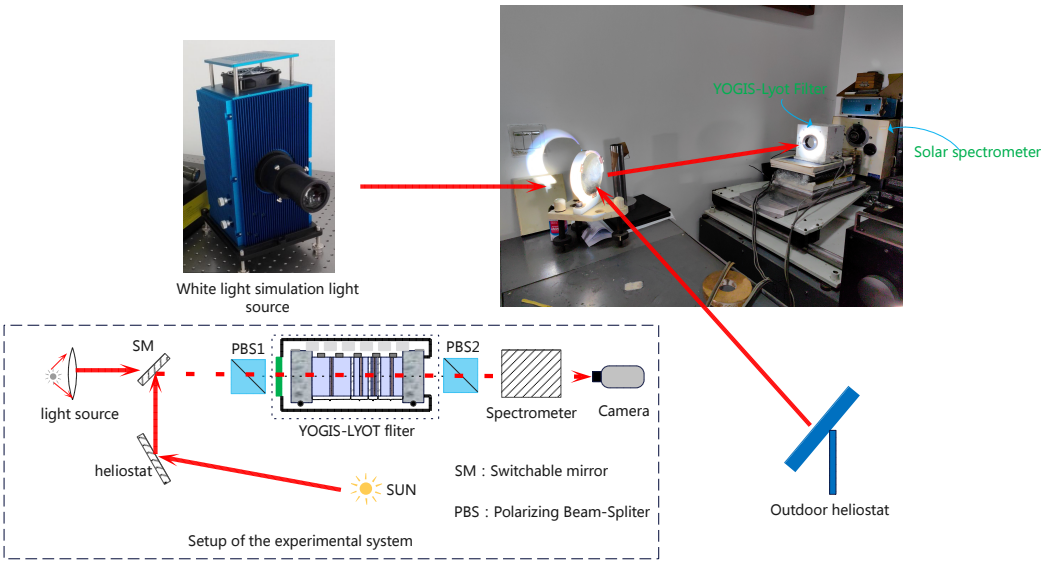


Figure 7. Experimental setup for the transmission band wavelength calibration of the YOGIS-Lyot filter.

2.7.2. Calibration Workflow

The workflow follows a "profile alignment → wavelength correction" two-step process, tailored to the filter's two-stage cascaded structure (1 Å, 2 Å units):

1. Transmission profile alignment:
   - Fix the driving voltage of the 2 Å Lyot unit (2–4 V) to maintain a stable reference transmission band.
   - Adjust the LCVR voltage of the 1 Å unit to shift its transmission band until it aligns with the 2 Å unit—resulting in a symmetric main peak, maximum peak intensity, and minimal sideband leakage.
2. Wavelength zero-point correction:
   - Calculate the wavelength offset ($\Delta\lambda$) between the aligned peak and the reference 5303 Å zero-point.
   - Use Equation (9) ($\Delta\lambda = \frac{\lambda_0^2}{\pi d_0 (n_o - n_e)} \Delta\delta$) to compute the required $\Delta\delta$ for LCVRs, then adjust voltages via calibrated coefficients to center the transmission band at 5303 Å.

2.7.3. Statistical Analysis of the Errors on Filter Performance

For the YOGIS-Lyot filter, the crystal processing errors and assembly errors in each Lyot filter stage are fixed, and these errors can be compensated by adjusting the phase retardance generated by the LCVRs. Therefore, the performance of the four-stage Lyot filter mainly depends on the retardance control error and uniformity of the LCVRs at each stage. It is assumed that each Lyot filter stage needs to be adjusted to center its transmission band at the designed wavelength, and the LCVR retardance control errors follow a normal distribution. The peak-to-valley (PV) range of the retardance control error is defined as six times the standard deviation. Different PV ranges of LCVR retardance control errors exert varying impacts on the performance of the four-stage liquid crystal Lyot filter. Using the Monte Carlo simulation method, 1000 simulated filter profiles were generated for each control error range, and statistical measurements of their performance parameters were conducted [9,28].

The central position of the filter's transmission band profile follows a normal distribution with a mean value equal to the theoretical wavelength of 5303 Å, and its distribution

characteristics can be described by the standard deviation. However, the distributions of the FWHM, peak transmittance, and sidelobe ratio of the transmission band profile do not conform to a standard normal distribution. Thus, the width of the 99.5% confidence interval is used to characterize the distribution of these parameters. Table 3 presents the statistical results of the central wavelength position, FWHM, peak transmittance, and integrated sidelobe energy ratio of the transmission band profile for the four-stage Lyot filter under different phase retardance control errors.

Table 3. Distribution of key performance parameters of the YOGIS-Lyot filter under different retardance errors.

Retardance Error	Std of Center Wavelength	Peak Transmittance	FWHM	Sidelobe Proportion
5°	8.68×10^{-4} Å	0.24%	3.00×10^{-5} Å	0.15%
10°	1.74×10^{-3} Å	0.89%	1.00×10^{-4} Å	0.42%
20°	3.6×10^{-3} Å	1.83%	7.40×10^{-4} Å	1.93%

When the stability of the LCVR phase retardance is maintained within ±5°, the central wavelength shift in the filter transmission band is $\pm 8.68 \times 10^{-4}$ Å, the FWHM fluctuation range is 3.00×10^{-5} Å, the peak transmittance fluctuation range is 0.24%, and the integrated sidelobe energy fluctuation range is 0.15%. Notably, the peak transmittance and integrated sidelobe energy exhibit a strong correlation, as both are reflections of the energy distribution.

2.7.4. Calibration Results

After calibration, the filter's transmission band exhibits:

- Central wavelength accuracy: Deviation from 5303 Å is <0.1 Å, meeting the 1 Å FWHM requirement.
- Mode-specific phase settings: Calibrated δ_{LCVR} values for key observation modes are documented in Table 4 (e.g., Single mode: LCVR1 = −18°, LCVR2 = 40°; +0.45 Å wing: LCVR1 = 261°, LCVR2 = −0.5°), enabling direct recall during on-site observation.

This calibration ensures the filter can reliably switch between green line core, background, and wing bands—critical for Doppler shift calculation and SNR enhancement. Figure 8 shows the finally calibrated transmission band curves for the four wavelength bands. Figure 9 illustrates the final theoretical and measured transmission band curves of the YOGIS-Lyot filter. It is evident from the plot that the results are in reasonable agreement with the expected performance. In the single-peak mode, the tuning precision is approximately 0.05 Å. In the dual-peak mode, the tuning precision is also less than 0.2 Å.

Table 4. Phase retardation of LCVRs for several wavelengths in actual observations after calibration.

Mode	Retardation	
	LCVR1	LCVR2
Single	−18°	40°
Double	−18°	210°
−0.45 Å	63°	80.5°
+0.45 Å	261°	−0.5°
−1 Å	162°	130°
+1 Å	162°	−50°

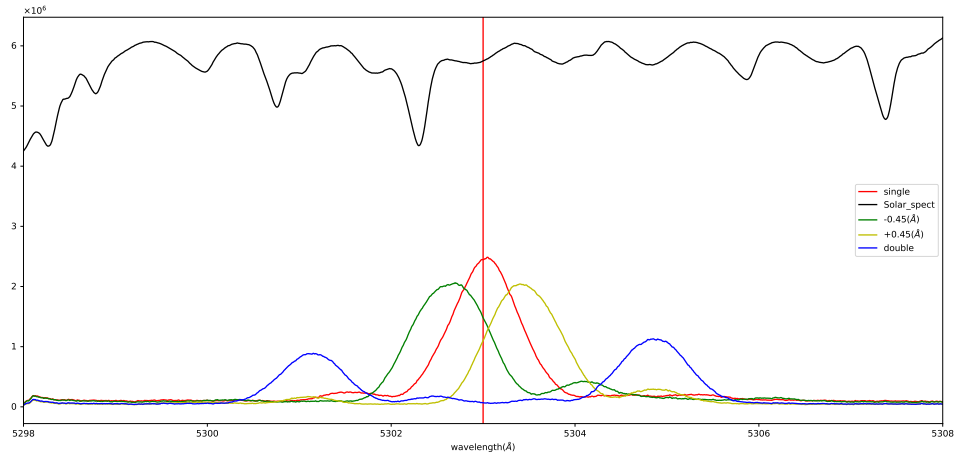
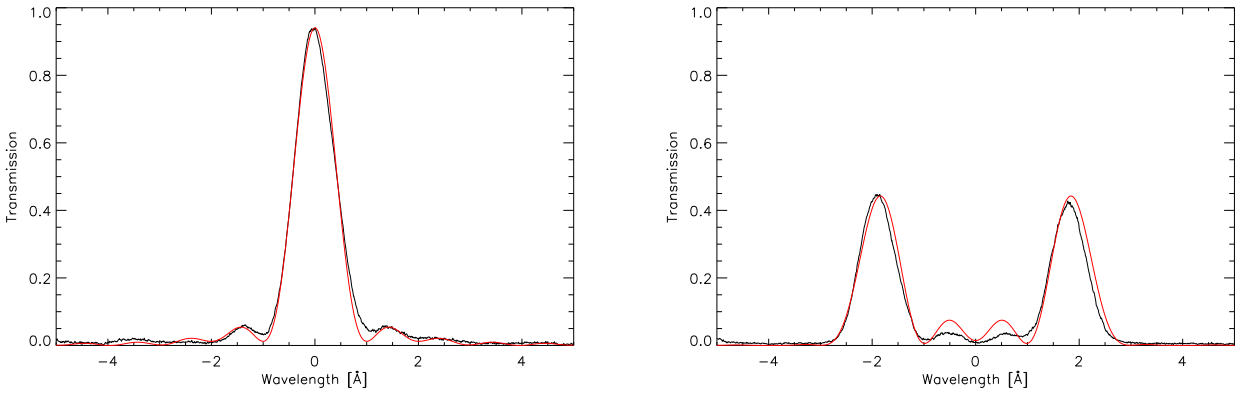


Figure 8. Practical transmission band curve of the YOGIS-Lyot filter at 5303 Å wavelength.



(**a**) Single-peak mode (**b**) Dual-peak mode

Figure 9. Measured vs. Theoretical Transmission Band Curves. The black curve represents the measured result, and the red curve represents the theoretical result.

2.8. Electronic Control System

The electronic control system of the YOGIS-Lyot filter is a core part of its design, providing stable thermostatic control and precise LCVR voltage regulation to support "fast-tunable" performance and long-term on-site reliability. The system is divided into two independent subsystems (Figure 10) to avoid cross-interference between temperature and voltage control.

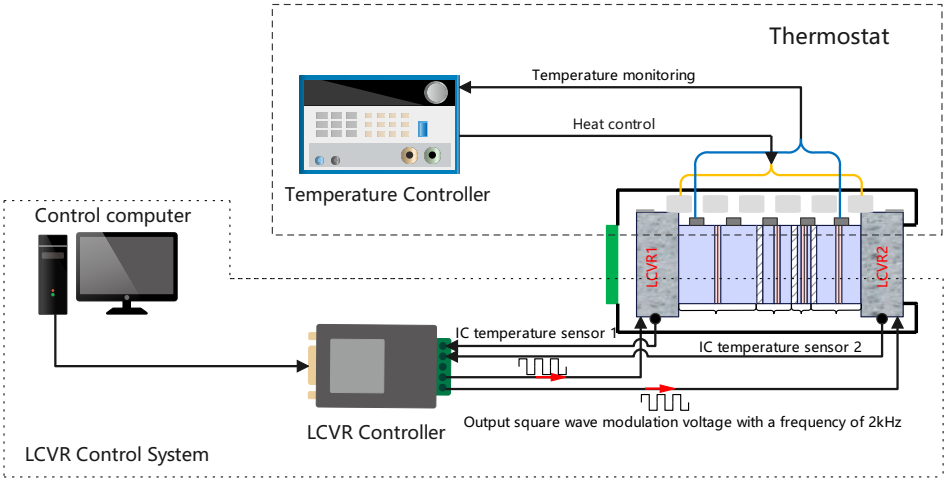


Figure 10. Electronic control system of the YOGIS-Lyot filter.

2.8.1. Thermostatic Control Subsystem

1. Design Rationale
   Temperature variations alter the wave plate length and refractive index, resulting in band shifts [13]:

$$\frac{\partial \lambda}{\partial T} = -\frac{\lambda}{\left(1 - \frac{\lambda}{\mu}\frac{\partial \mu}{\partial \lambda}\right)} \cdot \left(\frac{1}{\mu}\frac{\partial \mu}{\partial T} + \frac{1}{d} \cdot \frac{\partial d}{\partial T}\right) \quad (9)$$

   Around $\lambda = 5303$ Å, a temperature increase of 1 °C induces an approximate band shift of 0.3 Å in calcite. Therefore, for narrowband applications, to ensure the stability of the transmission band wavelength, it is generally necessary to equip a high-precision thermostatic device and house the entire filter assembly in a thermostat to enhance stability. As long as the temperature control accuracy of the thermostatic device is within 0.1 °C, the impact caused by temperature drift of the entire filter is negligible.
2. Hardware and Performance
   - Sensing and actuation: Three platinum resistance temperature detectors (RTDs) are embedded between the filter core sleeve and optical assembly to monitor temperature in real time. Heating resistors (wrapped around the sleeve) and a thermal insulation layer ensure uniform heating.
   - Control algorithm: A proportional–integral–derivative (PID) controller locks the chamber temperature at 40.6 °C (higher than Lijiang Observatory's ambient ~15 °C, enabling passive cooling) with a stability precision of 0.01 °C.
   - Integration: The subsystem connects to the host computer via a reserved RS232 interface, enabling remote temperature monitoring and parameter adjustment.

2.8.2. LCVR Voltage Regulation Subsystem

1. Design Constraints and Solutions
   LCVR liquid crystal molecules are damaged by long-term DC exposure; thus, the subsystem uses AC square-wave signals (2 kHz frequency, 50% duty cycle) to avoid molecular orientation degradation. The 2 kHz frequency exceeds the liquid crystal response speed (1 ms), ensuring stable δ_{LCVR} control.
2. Hardware and Performance
   - Signal generation: A custom FPGA-based multi-channel signal generator provides ±10 V adjustable amplitude signals, with 16-bit AD converters enabling 1 mV voltage resolution and <5 mV DC offset (via automatic DC balance).
   - Temperature feedback: Two integrated temperature sensors (attached to LCVRs) monitor real-time LCVR temperature, enabling dynamic voltage compensation via Equation (8) to counter thermal drift.
   - Expandability: The system supports six-channel waveform output (for future filter upgrades) and communicates with the host computer via RS232, enabling synchronized control with the YOGIS v1.0 observation software.

2.8.3. System Integration

The thermostatic and voltage subsystems are housed in compact, lightweight enclosures (Figure 11) to facilitate integration into the YOGIS's optical bench. Reserved cable interfaces simplify maintenance, while the independent design ensures that LCVR voltage tuning does not disrupt temperature stability—laying the hardware foundation for fast, reliable on-site observation.

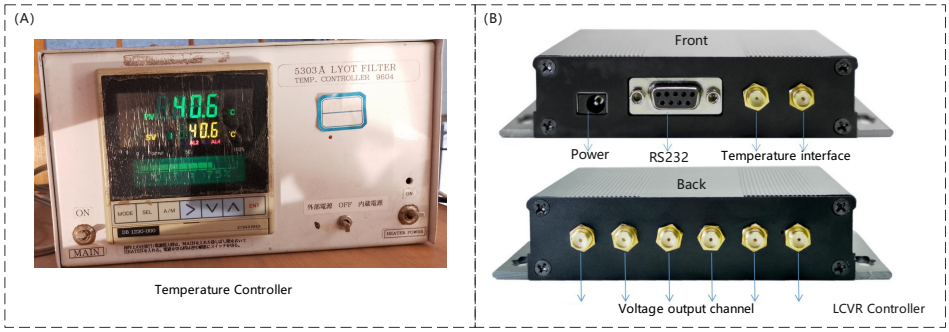


Figure 11. (**A**) Photographs of the thermostatic controller; (**B**) LCVR voltage modulation module for the YOGIS-Lyot filter.

3. On-Site Validation with the YOGIS

To thoroughly assess the practical performance of the LCVR-driven fast-tunable YOGIS-Lyot filter, a fundamental component designed for the YOGIS, on-site validation was performed at the Lijiang Observatory (Yunnan, China; altitude: 3200 m, geographic coordinates: 100°01′ E, 26°44′ N). The experiment systematically examined three essential performance metrics: compatibility with the YOGIS, wavelength tuning accuracy under field conditions, and the ability to capture high-SNR coronal green line images. Each of these metrics is critical for achieving the filter's intended scientific objectives.

3.1. Validation System Configuration

The YOGIS is a 10 cm aperture internal-occulting instrument optimized for observing the inner corona, featuring a native spatial resolution of 2.75 arcseconds per pixel. The YOGIS-Lyot filter was incorporated into the collimated optical path of the YOGIS coronagraph (Figure 12), with essential system components meticulously aligned to ensure perpendicular light incidence (alignment accuracy: <0.1°), thereby preventing degradation of polarization interference. The thermostatic chamber of the filter was maintained at 40.6 °C (temperature stability: ±0.01 °C), consistent with the calibration environment to mitigate thermally induced wavelength drift. The control system of the YOGIS-Lyot filter is integrated with the YOGIS observation system, facilitating coordinated control of multiple devices and the acquisition of coronal images across various wavelength bands. As illustrated in Figure 13, this integration is achieved through the coronagraph's integrated observation software interface, which was utilized for the entire on-site validation.

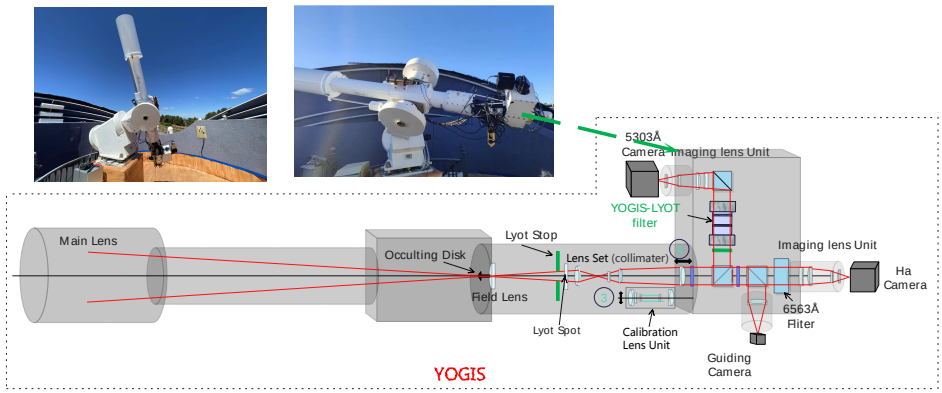


Figure 12. Installation Position of the YOGIS-Lyot Filter in the YOGIS Optical Path and Photographs of Actual Observation. The YOGIS-Lyot filter is mounted in the collimated optical path of the YOGIS coronagraph, as indicated by the green text annotation in the figure. PBS Prisms are placed at both its front and rear ends, enabling simultaneous observation of two wavelength bands.

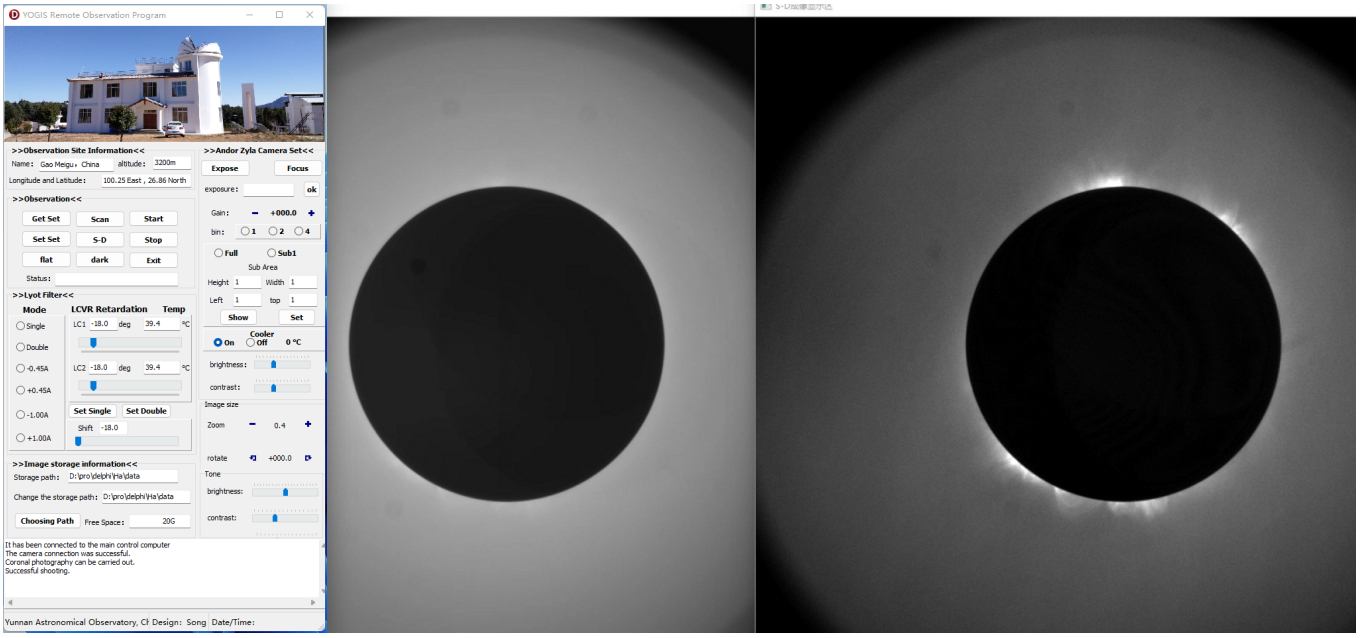


Figure 13. Interface of the Integrated Test Software v1.0 for the YOGIS coronagraph.

3.2. Validation Methodology

The validation workflow was designed to directly map to the filter's key design goals. The detailed protocol is as follows:

1. System Preparations: The YOGIS was aligned with the Sun to ensure stable light input. The filter's thermostatic chamber was preheated for 2 h to reach thermal equilibrium; calibration coefficients and target LCVR phase retardation values were loaded into the control software for one-click mode switching.
2. Multi-Mode Sequential Imaging: Leveraging the filter's fast-tuning capability, four key observation bands were captured in sequence (total imaging time: <10 s per cycle to avoid solar activity drift).
3. Image Post-Processing:
    - Dark current correction: Dark-field images (telescope cover closed, same exposure time) were subtracted to eliminate sensor noise.
    - Background subtraction: S-D (Single-Double) image fusion was performed to suppress atmospheric scattered light and instrumental stray light.
    - SNR quantification: SNR was calculated as $SNR = \frac{u_S - u_B}{\sigma_B}$, where u_S = mean gray value of coronal signal regions, u_B = mean gray value of off-limb background regions, and σ_B = standard deviation of the background.

3.3. Validation Results

Validation was conducted on 15 October and 20 October, 2024 (solar activity level: low, sunspot number: 7), as well as on 2 November 2024 (solar activity level: moderate, sunspot number: 23), with representative results shown in Figure 14 (single-mode coronal images) and Figure 15. Key outcomes are as follows:

1. Wavelength Tuning Accuracy and Speed
    - Tuning accuracy: Spectral analysis showed that the filter's actual central wavelength deviated by <0.2 Å (single-peak mode, <0.05 Å, dual-peak mode, <0.2 Å) from the target in all modes—consistent with the transmission band calibration results, confirming the effectiveness of the LCVR calibration and temperature compensation model.

- Tuning speed: The average switching time between any two modes was 50 ± 8 ms, meeting the design requirement (<60 ms) and outperforming traditional mechanical-tunable filters (switching time: 10–20 s). This fast tuning enabled sequential imaging of four bands within 10 s, avoiding artifacts from coronal loop evolution.

2. Image SNR and Quality
   - Core mode (single mode): SNR of coronal loops in the $1.03R_{\odot} \sim 1.5R_{\odot}$ range reached 35 ± 7 (low solar activity) and 42 ± 5 (moderate solar activity)—a 2.3 and 2.1 improvement, respectively, compared to the original YOGIS (SNR: 15 ± 3). This validates the filter's 1 Å FWHM narrowband transmission and background suppression capability.
   - Wing modes: The calculation of the Doppler velocity field is given by: $v = \frac{\Delta\lambda}{\lambda_0} \cdot c$, where v denotes the Doppler velocity, $\Delta\lambda$ represents the wavelength shift of the spectral line, λ_0 is the central wavelength of the spectral line in the rest frame, and c stands for the speed of light. Residual asymmetry between the $\pm$0.45 Å wings may introduce Doppler velocity bias. The Doppler velocity v exhibits a linear proportional relationship with the spectral line wavelength shift $\Delta\lambda$. The line wing employs single-peak modulation with a modulation error of less than 10%, and the deviation of the Doppler velocity field is also within 10%. Through the superposition processing of multiple images, this deviation will not affect the calculation results. Despite weaker line wing emission, the SNR of $\pm$0.45 Å wing images remained 19 ± 3 (low activity) and 22 ± 4 (moderate activity)—sufficient for Doppler shift calculation. Figure 16 presents the measured image of the coronal Doppler velocity field.
   - Background suppression: The S-D fused images reduced background noise by 72% compared to single-mode images alone, enabling detection of weak coronal plumes in the $1.5R_{\odot} \sim 2.5R_{\odot}$ range (previously undetectable with the original system).

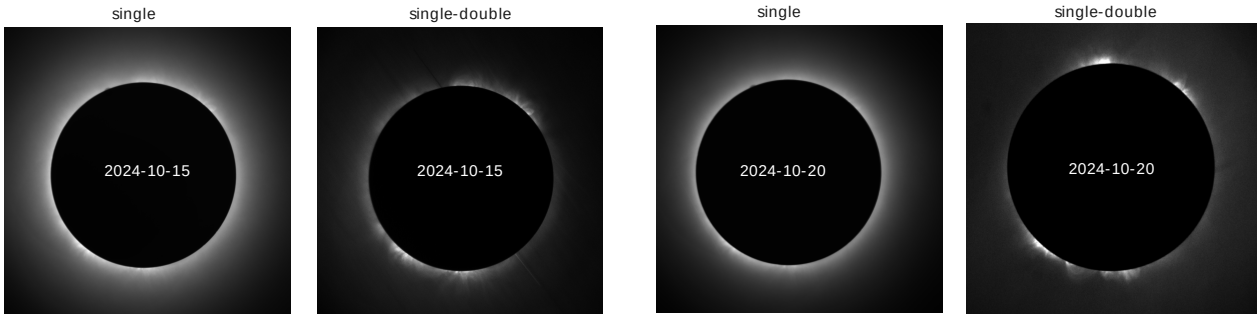


Figure 14. Sample images of the "single" band and "single-double" band acquired on 15 October and 20 October 2024. Background subtraction significantly improves the SNR of the images, enabling clearer visualization of inner coronal structures.

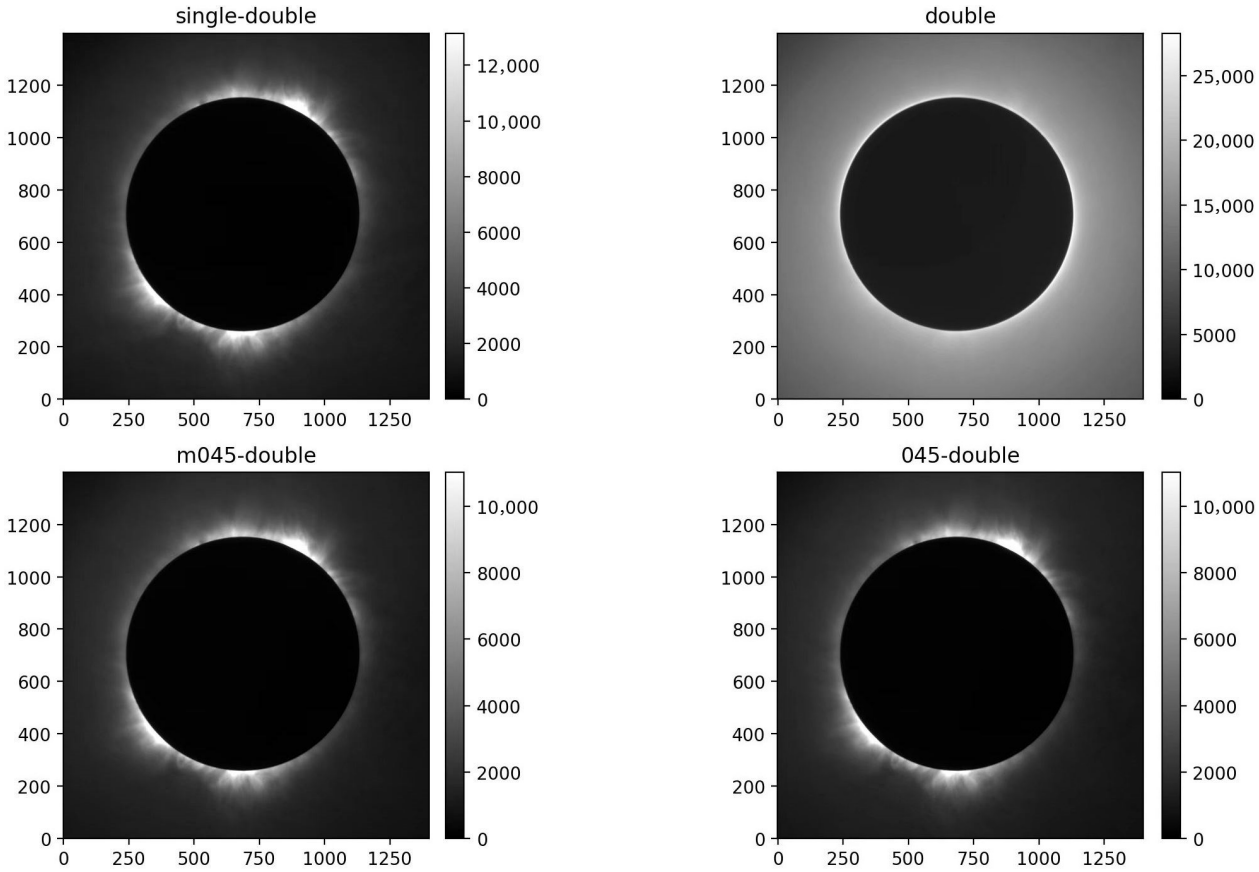


Figure 15. Sample images of four wavelength bands acquired on 2 November 2024. Arranged from top-left to bottom-right are the "single-double", "double", "m045-double", and "045-double" bands. Combined, these four bands enable the calculation of the Doppler velocity field. The images demonstrate the stable performance of the YOGIS-Lyot filter across all bands, fully meeting the requirements of coronal observations.

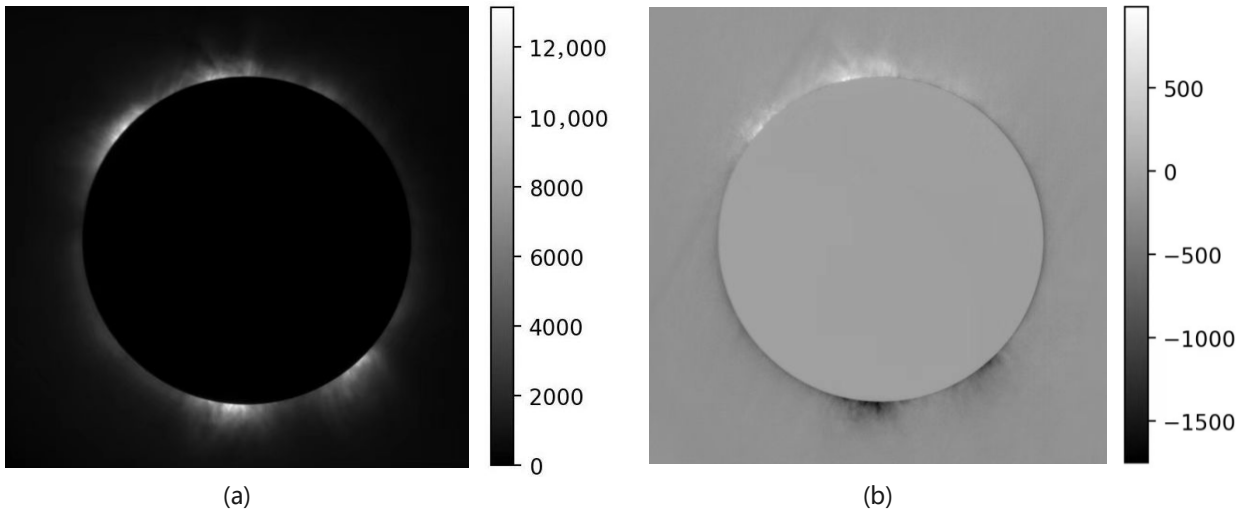


Figure 16. Doppler Velocity Field Images. (**a**) Processed image of the coronal green line acquired on 1 November 2024; (**b**) Doppler velocity field image processed on the same day. These images clearly reveal the distinct motion direction of the corona.

4. Conclusions

This study details the systematic design, high-precision calibration, and successful on-site validation of an LCVR-driven fast-tunable Lyot filter (YOGIS-Lyot filter) specifically

developed for the Yunnan Observatories YOGIS coronagraph at Lijiang Observatory. By addressing essential requirements for ground-based observations of the coronal green line—such as narrowband filtering, rapid wavelength tuning, and SNR imaging—the filter effectively overcomes the limitations associated with traditional mechanical-tunable Lyot filters, thereby fulfilling the intended scientific and technical objectives. The key conclusions are as follows:

- The optical design of the filter is fundamental to its exceptional performance. By employing a four-stage cascaded structure (FWHMs: 1 Å, 2 Å, 4 Å, 8 Å) in conjunction with two nematic liquid crystal variable retarders (LCVRs), the system achieves non-mechanical wavelength tuning. This design mitigates sensitivity to vibrations and the slow switching associated with mechanical systems, resulting in a tuning range of $\pm$2 Å centered around 5303 Å and a tuning time of less than 60 ms. The compact and lightweight optical assembly, combined with a thermostatic chamber, facilitates seamless integration with the 10 cm aperture YOGIS coronagraph while ensuring stable operation in high-altitude (3200 m) environments and under significant diurnal temperature variations.
- A two-step calibration workflow guarantees precise regulation of wavelength. The calibrated phase retardation values for key modes (Single, Double, $\pm$0.45 Å wings) facilitate one-click switching during on-site observations, thereby ensuring reliable performance.
- On-site validation at the Lijiang Observatory confirmed the filter's full compatibility with the YOGIS optical system, thereby enabling rapid multi-band sequencing of the green-line core, wings, and sky-background channels. The resulting coronal images exhibit a notable enhancement in performance, with the core-band signal-to-noise ratio (SNR) improving by a factor of 2–2.3 compared to the original system. Background-suppressed images obtained in single–double mode further reveal faint coronal structures extending to $2.5R_{\odot}$, thereby validating the effectiveness of the fast-tuning and dual-channel acquisition strategy. The integration of the filter's control system with the YOGIS observation software allows for coordinated multi-device control, thereby facilitating the efficient acquisition of coronal images and Doppler velocity field data.

Future research will concentrate on upgrading pre-filters to suppress secondary bands, optimizing exposure parameters to enhance wing-mode signal-to-noise ratio (SNR), expanding the tuning range to include the coronal red line, and developing an in situ automated calibration module. In summary, the YOGIS-Lyot filter successfully combines rapid tuning, high precision, and robust stability, offering a dependable technical solution for narrowband coronal imaging. Its design, calibration, and integration methodologies can be applied to other ground-based or space-borne coronagraphs, thereby advancing solar physics research and enhancing space weather monitoring capabilities.

Author Contributions: Conceptualization, Z.L. and Y.L.; methodology, T.S., M.Z. and Z.L.; data collection, X.Z. and M.Z.; experiments, T.S., X.Z. and M.Z.; writing—original draft preparation, T.S.; visualization, T.S.; writing—review and editing, Z.L.; funding acquisition, Z.L. All authors have read and agreed to the published version of the manuscript.

Funding: This work was jointly supported by multiple funding sources. Specifically, it received partial support from the National Natural Science Foundation of China (NSFC 12473089, 12373063, U2031148, 11873092, 11973086, 12173086, 12163004, and 11873090). Additionally, financial assistance was provided by the Yunnan Fundamental Research Projects (202401AT070140) and the Fundamental Research Funds for the Central Universities (No.: 2682025CX031).

Data Availability Statement: Data are contained within the article.

Acknowledgments: We are grateful to the project of the Yunnan Key Laboratory of Solar Physics and Space Science. We thank the anonymous referees for helpful comments and suggestions on the manuscript.

Conflicts of Interest: The funders had no role in the design of the study; in the collection, analyses, or interpretation of data; in the writing of the manuscript; or in the decision to publish the results.

References

1. Gong, Q.; Socker, D. Theoretical study of the occulted solar coronagraph. In Proceedings of the Optical Systems Degradation, Contamination, and Stray Light: Effects, Measurements, and Control, SPIE, Denver, CO, USA, 15 October 2004; Volume 5526, pp. 208–219.
2. Zhang, H.X.; Lu, Z.W.; Xia, L.D.; Liu, H.; Li, P. Stray light suppressing of optical system in white light coronagraph. *Opt. Precis. Eng.* **2009**, *17*, 2371.
3. Sun, M.; Zhang, H.; Bu, H.; Wang, X.; Ma, J.; Lu, Z. Computation of the diffracted field of a toothed occulter by the semi-infinite rectangle method. *J. Opt. Soc. Am. A* **2013**, *30*, 2140–2149. [CrossRef] [PubMed]
4. Liu, D.Y.; Zhang, H.X.; Sun, M.Z.; Huang, Z.H.; Xia, L.D.; Liu, W.X.; Fu, H. A New Method for Monitoring Scattered Stray Light of an Inner-occulted Coronagraph. *Res. Astron. Astrophys.* **2024**, *24*, 025020. [CrossRef]
5. Zhang, X.F.; Liu, Y.; Zhao, M.Y.; Song, T.F.; Wang, J.X.; Li, X.B.; Li, Z.H. On the relation between coronal green line brightness and magnetic fields intensity. *Res. Astron. Astrophys.* **2022**, *22*, 075007. [CrossRef]
6. Beckers, J.M.; Dickson, L.; Joyce, R.S. Observing the sun with a fully tunable Lyot-Ohman filter. *Appl. Opt.* **1975**, *14*, 2061–2066. [CrossRef] [PubMed]
7. Kopp, G.A. Tunable birefringent filters using liquid crystal variable retarders. In Proceedings of the Polarization Analysis and Measurement II, SPIE, San Diego, CA, USA, 14 September 1994; Volume 2265, pp. 193–201.
8. Tomczyk, S.; Card, G.; Darnell, T.; Elmore, D.; Lull, R.; Nelson, P.; Streander, K.; Burkepile, J.; Casini, R.; Judge, P. An instrument to measure coronal emission line polarization. *Sol. Phys.* **2008**, *247*, 411–428. [CrossRef]
9. Wang, X. Study on the Measurement Method of Solar Photosphere Magnetic Field Based on Liquid Crystal Filter. Ph.D. Thesis, University of Chinese Academy of Sciences, Beijing, China, 2023.
10. Bei, L.; Dennis, G.I.; Miller, H.M.; Spaine, T.W.; Carnahan, J.W. Acousto-optic tunable filters: Fundamentals and applications as applied to chemical analysis techniques. *Prog. Quantum Electron.* **2004**, *28*, 67–87. [CrossRef]
11. Glebov, A.L.; Mokhun, O.; Rapaport, A.; Vergnole, S.; Smirnov, V.; Glebov, L.B. Volume Bragg gratings as ultra-narrow and multiband optical filters. In Proceedings of the Micro-Optics 2012, SPIE, Brussels, Belgium, 8 May 2012; Volume 8428, pp. 42–52.
12. Cao, W.; Denker, C.J.; Wang, H.; Ma, J.; Qu, M.; Wang, J.; Goode, P.R. Characteristic evaluation of a near-infrared Fabry-Pérot filter for the InfraRed Imaging Magnetograph (IRIM). In Proceedings of the Telescopes and Instrumentation for Solar Astrophysics, SPIE, San Diego, CA, USA, 4 February 2004; Volume 5171, pp. 307–315.
13. Ai, G. Birefringent filter and its application to astronomy. *Prog. Astron.* **1987**, *5*, 317–329.
14. Shabtay, G.; Eidinger, E.; Zalevsky, Z.; Mendlovic, D.; Marom, E. Tunable birefringent filters—Optimal iterative design. *Opt. Express* **2002**, *10*, 1534–1541. [PubMed]
15. Miller, P.J.; Hoyt, C.C. Multispectral imaging with a liquid crystal tunable filter. In Proceedings of the Optics in Agriculture, Forestry, and Biological Processing, SPIE, Boston, MA, USA, 6 January 1995; Volume 2345, pp. 354–365.
16. Hou, J.F.; Deng, Y.Y.; Wang, D.G.; Lin, J.B.; Zhang, Y.; Sun, W.J.; Zhang, Z.Y.; Sun, Y.Z. Application and prospect of liquid crystal modulation technology in solar magnetic field detection. *Spacecr. Environ. Eng.* **2021**, *38*, 296–304.
17. Hagino, M.; Ichimoto, K.; Kimura, G.; Nakatani, Y.; Kawate, T.; Shinoda, K.; Suematsu, Y.; Hara, H.; Shimizu, T. Development of a universal tunable filter for future solar observations. In Proceedings of the Advances in Optical and Mechanical Technologies for Telescopes and Instrumentation, SPIE, Montréal, QC, USA, 28 July 2014; Volume 9151, pp. 1977–1984.
18. Liu, Y.; Zhang, X. The coronal green line monitoring: A traditional but powerful tool for coronal physics. *Proc. Int. Astron. Union* **2018**, *13*, 169–170. [CrossRef]
19. Sha, F.; Liu, Y.; Zhang, X.; Song, T. Characterization and correction of the scattering background produced by dust on the objective lens of the Lijiang 10-cm coronagraph. *Sol. Phys.* **2023**, *298*, 139. [CrossRef]
20. Song, T.; Liu, Y.; Zhang, X.; Zhao, M.; Li, X.; Luo, Q.; Sha, F.; Liu, Q.; Oloketuyi, J.; Wang, X. Toward Automated Coronal Observations: A New Integrated System Based on the Lijiang 10 cm Coronagraph. *Universe* **2025**, *11*, 154. [CrossRef]
21. Xin, Y.X.; Bai, J.M.; Lun, B.L.; Fan, Y.F.; Wang, C.J.; Liu, X.W.; Yu, X.G.; Ye, K.; Song, T.F.; Chang, L.; et al. Astronomical site monitoring system at Lijiang observatory. *Res. Astron. Astrophys.* **2020**, *20*, 149. [CrossRef]
22. Ichimoto, K.; Noguchi, M.; Tanaka, N.; Kumagai, K.; Shinoda, K.; Nishino, T.; Fukuda, T.; Sakurai, T.; Takeyama, N. A new imaging system of the corona at norikura. *Publ. Astron. Soc. Jpn.* **1999**, *51*, 383–391. [CrossRef]

23. Wang, X.; Liang, Y.; Zhang, J.; Wu, J.; Yuan, S.; Fu, Y.; Lü, Z.; Mao, W.; Jin, Z. Development of Rapid Tunable Lyot Filter and Its Observation on 1 m New Vacuum Solar Telescope. *Acta Opt. Sin.* **2023**, *43*, 2423001.
24. Optics, M. Meadowlark Optics. Available online: https://www.meadowlark.com/ (accessed on 7 March 2019).
25. Gu, N.; Chen, H.; Tang, A.; Fan, X.; Noda, C.Q.; Xiao, Y.; Zhong, L.; Wu, X.; Zhang, Z.; Yang, Y.; et al. Embedded solar adaptive optics telescope: Achieving compact integration for high-efficiency solar observations. *Opto-Electron. Adv.* **2025**, *8*, 250025. [CrossRef]
26. Yang, J.; Tang, A.; Lian, B.; Xiong, Z.; Ma, Z.; Gu, N. Optimal multi-spectrum polarization detection with full-Stokes in a single channel by using standard retarders. *Measurement* **2025**, *242*, 116052.
27. Hou, J.; Sun, Y.; Lin, J.; Zhang, Y.; Wang, D.; Deng, Y.; Zhang, Z. In Situ Calibration of the Tunable Liquid-crystal Birefringent Filter. *Acta Photonica Sin.* **2023**, *52*, 0552208.
28. Frenkel, D.; Smit, B. *Understanding Molecular Simulation: From Algorithms to Applications*; Elsevier: Amsterdam, The Netherlands, 2023.

Disclaimer/Publisher's Note: The statements, opinions and data contained in all publications are solely those of the individual author(s) and contributor(s) and not of MDPI and/or the editor(s). MDPI and/or the editor(s) disclaim responsibility for any injury to people or property resulting from any ideas, methods, instructions or products referred to in the content.